metals

MDPI

Article

High Cycle Fatigue and Range-Mean Performance of Emerging Titanium Alloys for Aeroengine Applications

Peter Davies [1], Sean John [1], Helen Davies [1], Martin Bache [1,*], Kate Fox [2], Christopher Collins [2], Nigel Martin [2] and Rebecca Sandala [2]

[1] Institute of Structural Materials, Swansea University, Bay Campus, Fabian Way, Crymlyn Burrows, Swansea SA1 8EN, UK; p.d.davies@swansea.ac.uk (P.D.); s.e.john@swansea.ac.uk (S.J.); h.m.davies@swansea.ac.uk (H.D.)

[2] Rolls-Royce plc, P.O. Box 31, Derby DE24 8BJ, UK; katharine.fox@rolls-royce.com (K.F.); nigel.martin@rolls-royce.com (N.M.); rebecca.sandala@rolls-royce.com (R.S.)

* Correspondence: m.r.bache@swansea.ac.uk

Abstract

Four alpha-beta titanium alloys, containing increased beta stabilising elements when compared to the well established Ti-6Al-4V, were previously characterised for their low cycle fatigue behaviour and resistance to cold dwell sensitivity. The same four alloys are now assessed for high cycle fatigue performance, employing plain cylindrical and notched specimen geometries. Fatigue strength under load-controlled cycling was measured under two contrasting mean stress conditions, a fully reversed R = −1 waveform and a positive mean stress waveform of R = 0.3. The role of microstructure and micro-texture are considered to explain the relative high cycle fatigue behaviour of each alloy and in particular the mechanisms responsible for fatigue crack initiation. The data are subsequently employed to construct "safe stress" range-mean diagrams.

Keywords: titanium alloys; high cycle fatigue; notch fatigue; range-mean behaviour

1. Introduction

The aero-engine engineering sector has continually sought to extend the mechanical capabilities of titanium alloys in order to improve gas turbine safety and efficiency. Most recently, the need for materials sustainability and economical component processing has prompted increasing efforts in novel powder metallurgy techniques and the development of wrought products with improved formability [1].

Titanium alloys are usually classified according to their elemental additions and whether these stabilise the allotropic α or β phases at room temperature [2]. Aerospace-grade titanium alloys offer significant mechanical properties which are tailored via precise thermo-mechanical processing [3–7]. The resultant microstructures, combined with crystallographic texture, intimately control the static and cyclic mechanical properties of these alloys [8–10].

Titanium alloys have been widely employed in the compressor section of gas turbines since the 1950s and have become routinely selected for critical rotating components and containment structures [11,12]. Advanced applications now include integrally bladed discs (blisks) [13,14] that provide notable weight savings over traditional disc designs incorporating mechanically attached blades.

The well established Ti-6Al-4V (Ti-6-4) continues to be the most commonly utilised α + β alloy in commercial and military engine applications, still accounting for over 50% of

Academic Editor: Tarun Goswami

Received: 27 April 2026
Revised: 27 May 2026
Accepted: 4 June 2026
Published: 8 June 2026

all global titanium alloy production [15]. However, with future engineering applications in mind, recent research has focussed upon the development of alternative titanium alloys with improved processing capabilities and potentially superior fatigue performance. One line of investigation has been to increase the level of β phase stabilisation, thus lowering the β transus temperature, improving formability and ultimately increasing ductility. A recent study concentrated upon the low cycle fatigue (LCF) and associated dwell fatigue sensitivity of four such alloys [16]. Whilst providing an essential background to their static and fatigue strengths, additional aspects of fatigue behaviour must also be considered.

Rotating disc components with relative thick section sizes are primarily designed for optimum LCF performance. In contrast, compressor aerofoils in particular experience life limiting vibratory loads which have been implicated as a prime cause of past engine failures in operational aircraft [17]. Such resonance behaviour can be simulated via high cycle fatigue (HCF) characterisation in the laboratory setting, through experiments designed to induce specimen failures between say 10^6 and 10^7 cycles of constant amplitude loading. HCF strength is intimately related to localised plasticity focussed around microstructural processing artifacts or features resulting from surface finishing. Crack initiation under HCF has been reported in various titanium alloys at stresses significantly below static yield and initiation sites regularly occur at sub-surface locations due to the influence of micro-texture or specific combinations of neighbouring crystallographic grains [18]. The advent of electro-mechanical rigs capable of testing samples under loading frequencies extending into the kilohertz range has enabled assessments into what is now termed very high cycle fatigue (VHCF). A range of key engineering alloys has been studied over the past three decades [19]. In the specific case of Ti-6-4, for example, which had hitherto displayed a single plateau and a distinct endurance stress at the extent of the SN curve out to say 10^7 cycles, the SN curve has been noted to display a secondary shelf when testing out to 10^9 cycles has been possible [20]. This can be highly pertinent to applications requiring long term service at high frequency.

In contrast to LCF scenarios, where (typically) low-frequency loading reversals facilitate mid-service inspections during the crack propagation stages, vibration or resonance loading results in limited time periods of sub-critical crack growth. This restricts "damage tolerant" inspection and associated lifing techniques [21]. Under high frequency HCF, cracks are able to propagate to their critical dimension in relatively short time (i.e., within a low number of flight or mission cycles). This is irrespective of the cause of cracking, i.e., whether initiated from cyclic damage, inherent processing defects or mechanical/impact/erosion damage to the component surface. In addition, the vibration is often superimposed upon a high static stress and it is accepted that high mean stress (high R) fatigue waveforms promote relatively fast growth and lower fatigue crack growth threshold levels [16]. Such knowledge has underpinned the development of modern "sub-threshold" design philosophies to avoid HCF component failures, i.e., service loading must not exceed the fatigue crack growth threshold (ΔK_{th}) condition [22,23].

Historically, more simplistic "safe stress" component lifing philosophies have been adopted for aerofoils [24]. Possibly more conservative in nature, these models rely on relatively standard fatigue testing of simple specimen geometries to ascertain fatigue strength over a variety of mean stress conditions. Accordingly, constant life or range-mean diagrams (RM) are generated [25]. This defines safe regimes of HCF loading under which a component should theoretically avoid failure within the cyclic lifetime under consideration. Traditionally, for conventional metallic alloys demonstrating a controlled degree of scatter in fatigue performance, the most basic of RM diagrams is constructed by first performing a single set of fatigue experiments to derive a stress-life curve (SN) employing a fully reversed ($R = -1$) waveform. The stress range that induces failure at specific magnitudes

of cyclic life (e.g., 10^6, 10^7 cycles etc) is then read off and plotted on the Y axis of the RM graph (i.e., reflecting measured HCF life under a mean stress of zero). The other extremity of the "Goodman line" (when assuming a linear RM relationship) is defined by the UTS or proof strength of the material (i.e., "failure" measured under a tensile load ramp where the alternating stress range equals zero) and is plotted on the X axis. Multiple "lines of constant predicted life" then radiate from the UTS data point, schematically represented in Figure 1 utilising a purely nominal set of data, allowing designers to interpolate safe RM conditions for an infinite number of untested R ratios. Figure 1 is annotated to highlight the key SN datapoints (DP1 to DP4) used to construct the RM diagram. More rigorous test programmes incorporating testing at intermediate R ratios could define additional points along the Goodman line. Safety factors are incorporated to the specific constant-life trendlines to establish the "safe stress" region, i.e., any combination of range and mean stress falling below the appropriate RM HCF life line.

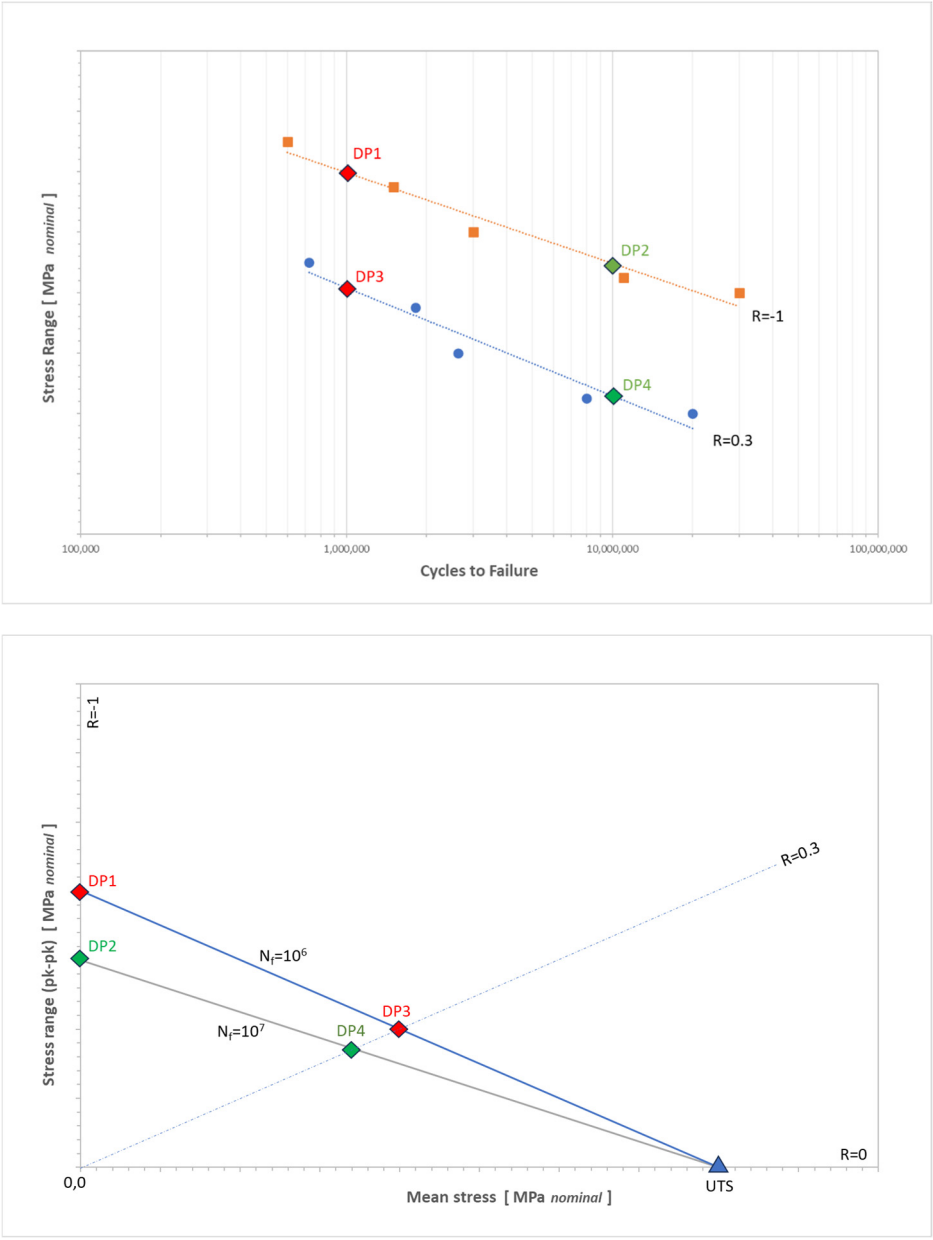

Figure 1. Using nominal HCF data generated at two mean stress conditions of R = −1 and R = 0.3 (**top**) for the construction of a linear RM Goodman diagram (**bottom**).

However, the simple Goodman straight line model is not appropriate when alloys are known to display a significant mean stress dependence [26]. Therefore, it is prudent to perform additional HCF tests under at least one other mean stress condition to instead generate a "Haigh curve" [27].

It is also pertinent to recognise that aeroengine components typically contain geometrical features such as notches, fillet radii and holes which can act as sites of stress concentration. Immediately adjacent to such features the local stress is greater than the nominal net section stress applied to the component. Fatigue failures of engineering components often occur from such stress raisers [28]. Therefore, HCF testing of specimens containing a notch (NHCF testing) is also essential to assess the supplementary impact of these features on fatigue properties.

The aim of the present research was to determine the HCF and NHCF performance of the same four titanium alloys previously studied [16]. Commercial sensitivities must again be considered; therefore, two of the alloys are simply referred to as Alloy A and Alloy B. These were produced on an industrial scale under established processing regimes. These are then compared with two additional alloys, namely S23 and RR11, which remain in the early stages of their development. Detailed fractography was performed to correlate HCF behaviour to microstructure and micro-texture. The fundamental constant amplitude HCF data were subsequently analysed to construct range-mean, safe stress prediction diagrams.

2. Experimental Methods

2.1. Materials

The four alloys studied here were the same as those assessed for low cycle fatigue performance in a recent report [16]. Precise descriptions of the thermo-mechanical processing routes, resultant microstructures, grain size distributions and micro-textures associated with each alloy are available in that previous publication. However, representative microstructures are reproduced in Figure 2. Metallographic images were prepared from mechanically cut sections, mounted in conductive bakelite, ground and polished to a final 0.04 µm finish using non-crystallising colloidal silica solution, then etched using Kroll's reagent. Notations refer to primary alpha grains (α_p), secondary alpha phase (α_s), transformed beta phase (β) and grain boundary alpha (GB_α). The image of alloy S23, as shown in Figure 2c, is deliberately included at a lower magnification to illustrate the scale of the relatively large grain size and sub-structure.

Alloy A was triple vacuum arc remelted (3xVAR) then thermo-mechanically worked down to 100 mm diameter bar and cut to 300 mm lengths. The alloy was then solution heat treated (STA) and water quenched, followed by an anneal at 700 °C for 2 h, before being air cooled to room temperature. Alloy A displayed a bimodal microstructure which often featured a continuous layer of grain boundary α.

Alloy B was plasma arc melted and vacuum arc remelted (PAM-VAR) and thermo-mechanically worked to produce a 100 mm diameter bar, cut to 300 mm in length, and then heat treated for 2 h at 760 °C before being air cooled. Alloy B was also found to have a bimodal microstructure; however, the transformed β grains notably contained coarse secondary α laths of several microns in width.

A 250 mm × 20 mm disc of S23 was produced at Sheffield University via the field-assisted sintering technology (FAST) process, combining a blend of Ti-6-4 and Ti-5553 powders [29]. This process supports the potential application of powder metallurgy (PM)-based titanium alloys in high performance engineering applications. Compared to other sintering-based processes, benefits include faster heating rates, lower sintering temperatures and/or shorter processing times, and elimination of sintering aids [30]. FAST also offers the ability to rapidly and consistently produce fully sintered, near net shape parts

with uniform density or controlled porosity, with consistent microstructure. Field-assisted sintering of the powder blend was performed at 1200 °C in the β phase field for 60 min, initially heated at a rate of 50 °C/min, which was then reduced to 25 °C/min for the last 150 °C to avoid overshooting. Post sinter, the alloy was slow cooled at a rate of 10 °C/min. S23 displayed an equiaxed lamellar microstructure where prior β grains usually consisted of packets of aligned α and β laths. The β grains were often enclosed by a layer of grain boundary α several microns in width.

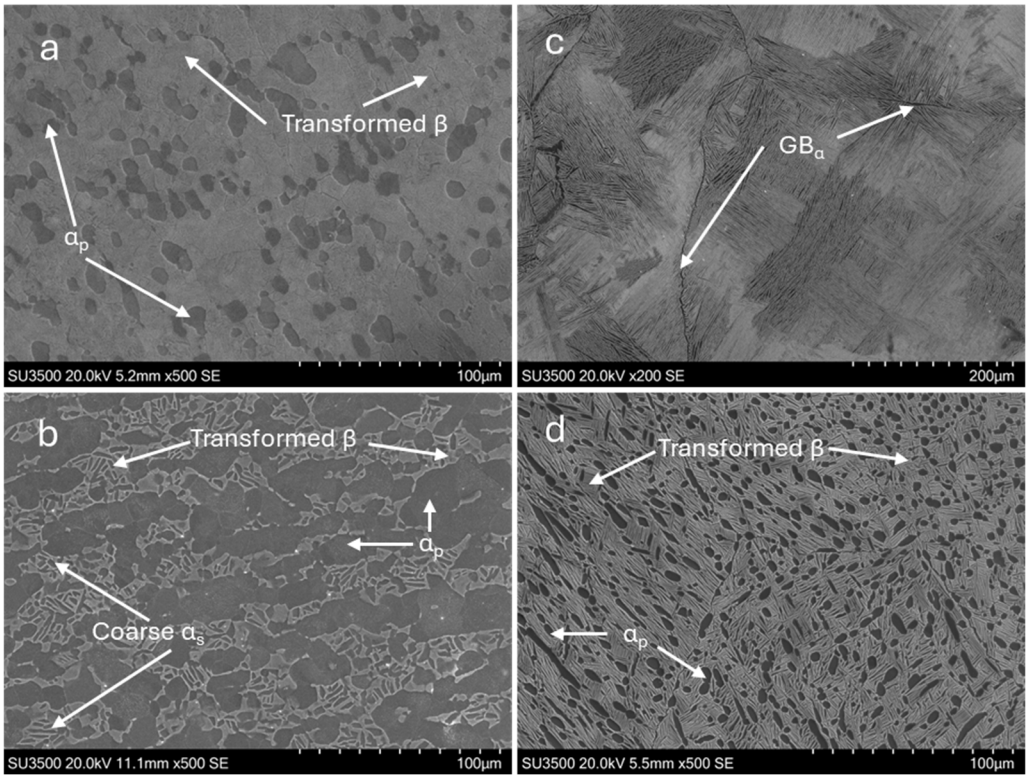

Figure 2. Microstructures of the four alloys to illustrate relative grain sizes and selected metallurgical phases (reproduced from ref. [16]): (**a**) Alloy A; (**b**) Alloy B; (**c**) S23; (**d**) RR11.

RR11 was induction skull melted (ISM) at Imperial College and centrifugally cast into 60 mm diameter moulds, which were then flat rolled at 860 °C. These were then heat treated at 860 °C for 6 h and vermiculite cooled to room temperature. The bars were then aged at 600 °C for 2 h, before being vermiculite cooled to room temperature. RR11 also had a bimodal microstructure with primary α grains contained in a transformed β matrix. The primary α grains were often found to be elongated. RR11 is the subject of a patent application [31].

Table 1 records the micro-texture measurements sampled for each alloy, employing a Hitachi SU3500 scanning electron microscope (SEM, Hitachi High-Tech Europe GmbH, Tokyo, Japan) equipped with EBSD capability (Aztec HKL version 5.1 software). The field of view was optimised for each individual alloy, in part according to the scale of the underlying microstructural features but mainly due to the quality of signal indexing.

The aluminium and molybdenum equivalence (Al. Eqv. and Mo. Eqv.) of Alloys A and B, S23 and RR11 are illustrated in Table 2. This emphasises the increased levels of β stabilisation in each when compared to Ti-6-4.

Table 1. Micro-texture intensities.

Alloy	Micro-Texture Intensity (Times Random)	Field of View (mm^2)
RR11	7.6	2.3
S23	6.3	4.8
Alloy A	5.8	1.0
Alloy B	1.7	3.3

Table 2. Equivalent Al. and Mo. contents compared to Ti 6-4 (Data from ref. [16]).

Alloy	Ti-6-4	Alloy A	Alloy B	S23	RR11
Al eqv. (%)	7	6.8	8.58	7.05	4.67
Mo eqv. (%)	2.5	5.28	2.61	6.65	4.64

2.2. Mechanical Testing

Plain cylindrical and double edged notched (K_t = 1.92) fatigue test specimens were manufactured from all four alloys, Figure 3. In the case of the plain specimens, the entire gauge surface was glass shot peened to a target Almen intensity of M0.44N and a coverage of 200%. End milling was employed to machine the formed finish of the semi-cylindrical notches in the DEN specimens, with the breaking edges radiused via a longitudinal polish.

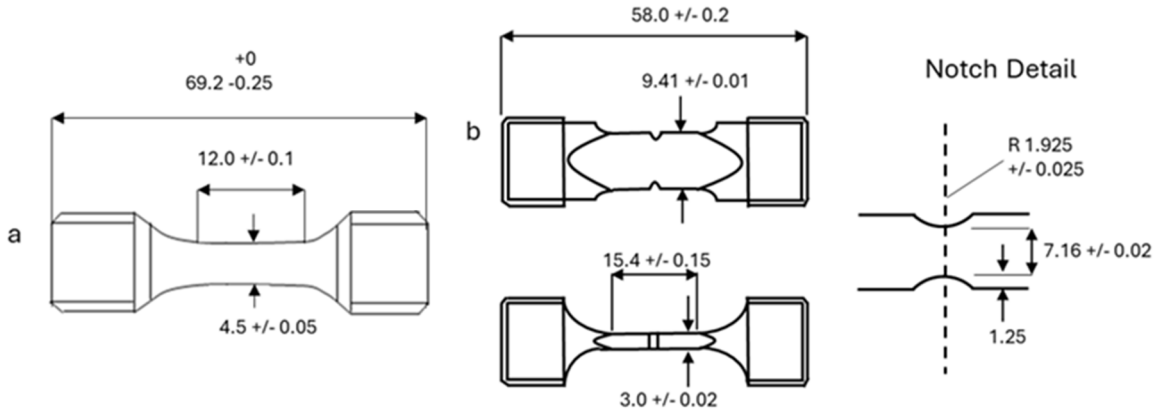

Figure 3. (**a**) Plain fatigue specimen; (**b**) notched fatigue specimen. Dimensions in mm.

HCF tests were performed in accordance with ISO 1099:2006 [32], employing a vibrophore electro-resonance fatigue machine (ZwickRoell GmbH & Co., Ulm, Germany) resonating at approximately 100 Hz. Tests were conducted at room temperature and at a mean stress condition of either R = 0.3 or R = −1 using a sinusoidal waveform. The number of different R ratios employed for assessment was restricted by the volumes of available materials. Naturally, R = −1 was selected with the ultimate construction of range-mean diagrams in mind. The positive mean stress waveform of R = 0.3 was then chosen to represent selected aerofoil operations. Material stocks allowed for a bare minimum of two specimens (usually three or greater) to define an SN curve under any specific specimen/R ratio combination. Occasionally, material stocks were sufficient to support repeat testing at a single applied stress condition.

Initially guided by the previous study of LCF strength [16], specimens were loaded under peak applied stress conditions aiming to generate fatigue failures within the life range 10^6 to 10^7 cycles. The majority of tests were performed under a single, constant amplitude load until failure. However, specimens surviving beyond 10^7 cycles were stepped up in 25 MPa increments for additional blocks of 10^7 cycles prior to eventually promoting failure.

The "endurance stress" from these step tests was then interpolated employing the following equation [33]:

$$\sigma_e = \sigma_{ps} + (\sigma_f - \sigma_{ps})(\frac{N_f}{N_{ro}}) \quad (1)$$

where σ_e = the endurance stress, σ_{ps} the stress from the block completed immediately prior to failure, σ_f the stress of the block inducing failure, N_f the number of cycles completed at σ_f and N_{ro} the number of cycles designated as the "run out" (i.e., 10^7, the number of cycles per stepped block). For tests where σ_e was interpolated using Equation (1) the interpolated stress data points are plotted on the SN graphs at 10^7 cycles with an arrow.

Fracture surfaces and polished microstructural sections were characterised employing optical and scanning electron microscopy. Cross sections were prepared employing mechanical cutting. Detailed information concerning the precise location and form of fatigue crack initiation sites was recorded.

3. Results

3.1. HCF Data: Plain Specimens

The HCF data obtained from plain specimens tested under loading ratios of R = −1 and R = 0.3 are plotted in Figures 4 and 5 respectively. The number of cycles to failure are plotted as a function of the peak applied stress, as calculated across the cylindrical cross-section area. It is evident that the stress levels applied to the majority of S23 specimens were often too high to generate failure lives exceeding 10^6 cycles. The interpolated endurance strength (Equation (1)) is plotted for step test specimens that achieved the run-out specification set at 10^7 cycles. These points are marked with an arrow. Best fit logarithmic trend lines are superimposed for each alloy data set in both figures, with the best fits extrapolated to a HCF life of 10^7 cycles where a step test was not generated.

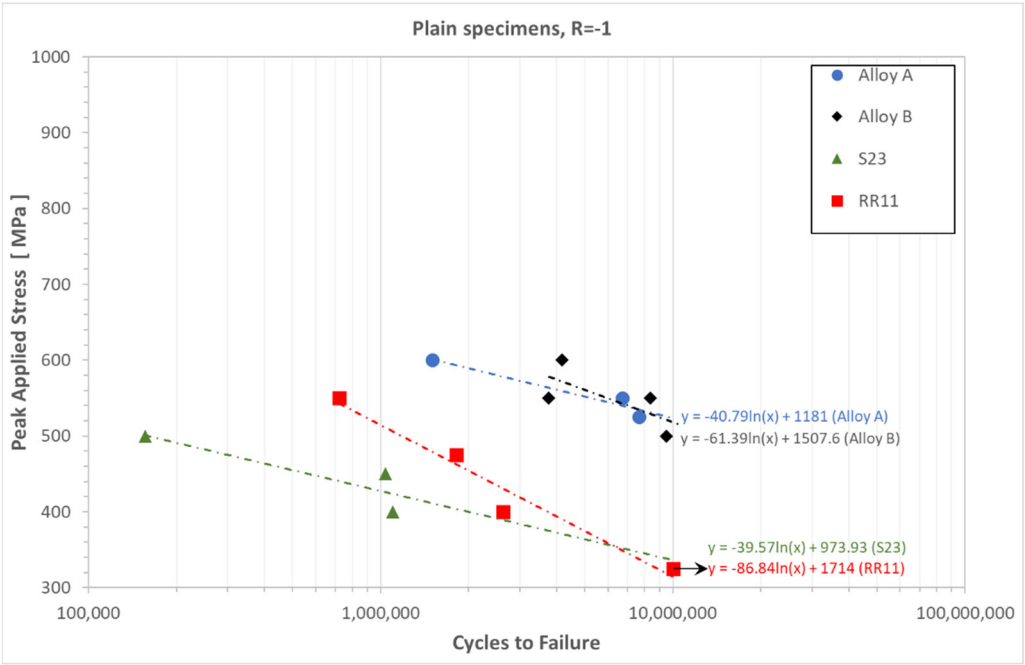

Figure 4. HCF data measured from plain specimens at R = −1 (20 °C, 100 Hz).

At R = −1 the HCF response of Alloy A and Alloy B was very similar. Under this scenario two tests were performed on Alloy B at 550 MPa, indicating an approximate x2 scatter factor in the life to failure. At R = 0.3 Alloy A was clearly superior in strength when

compared to any other alloy. In comparison, at both R ratios, RR11 and S23 demonstrated relatively low fatigue strengths.

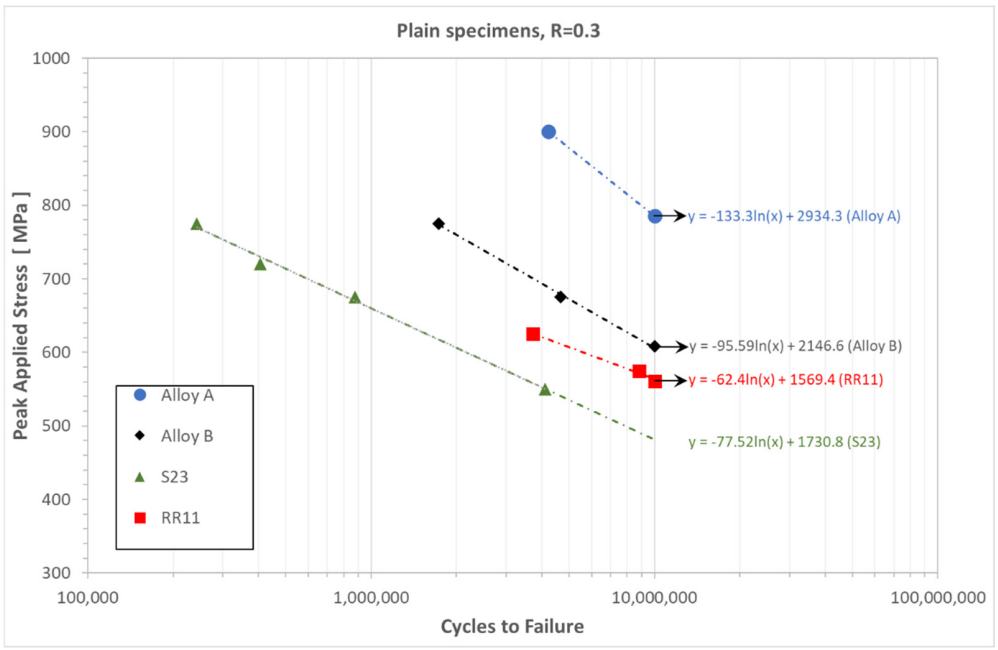

Figure 5. HCF data measured from plain specimens at R = 0.3 (20 °C, 100 Hz).

3.2. HCF Data: Notch Specimens

The HCF data obtained from notch specimens tested under loading ratios of R = −1 and R = 0.3 are plotted in Figures 6 and 7 respectively. The number of cycles to failure are plotted as a function of the peak applied stress, calculated across the orthogonal, net cross-section between the opposing notches. No accounting for the stress concentration effect of the notches has been taken. Once again, the interpolated endurance strength (Equation (1)) is plotted for step test specimens that achieved the run-out specification set at 10^7 cycles. These points are marked with an arrow.

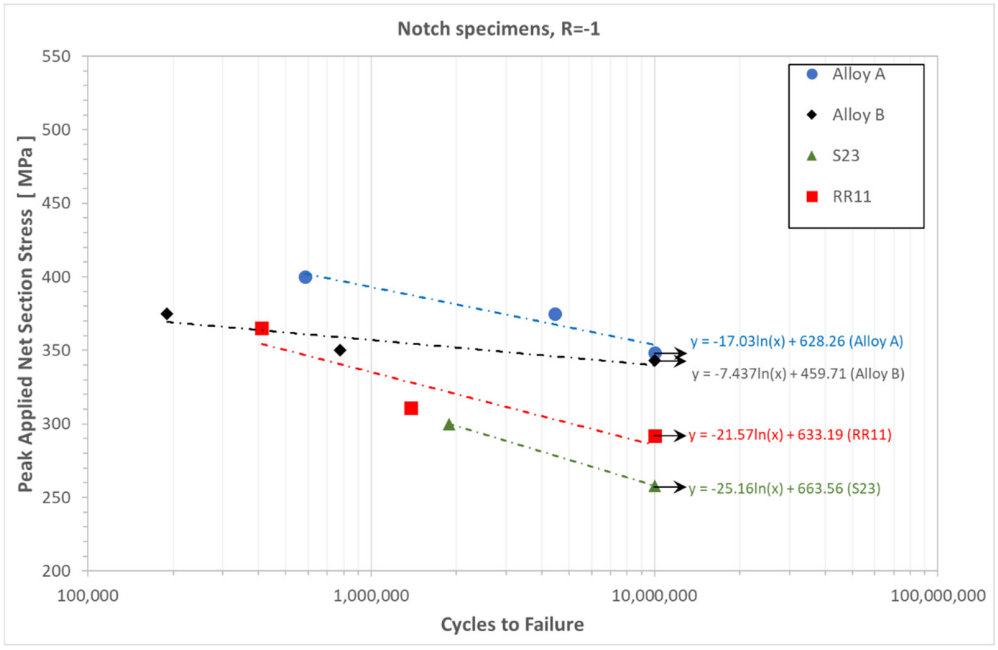

Figure 6. HCF data measured from notch specimens at R = −1 (20 °C, 100 Hz).

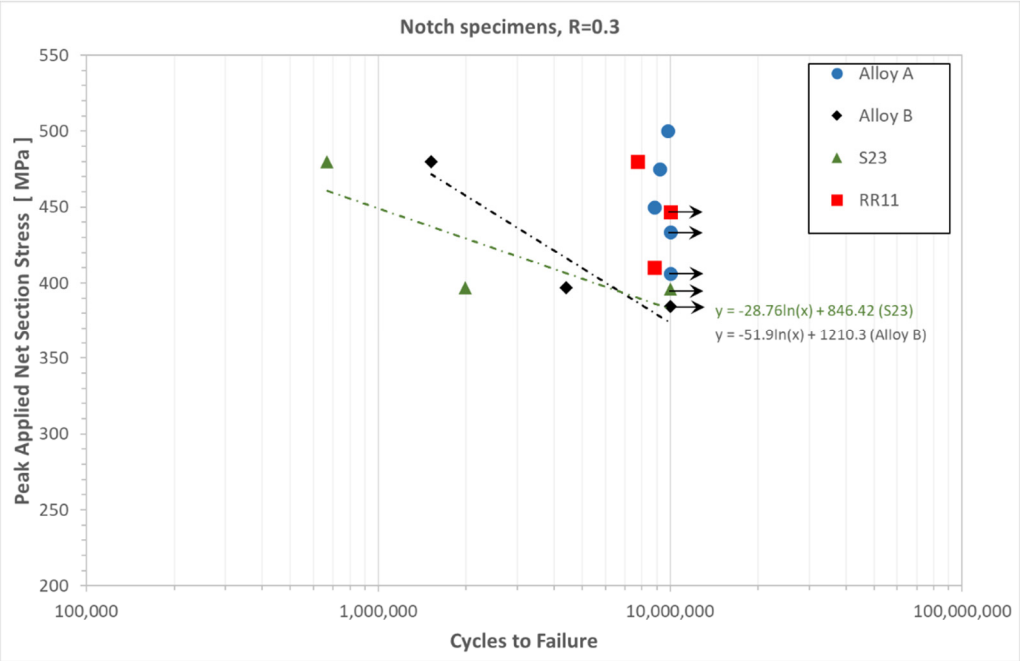

Figure 7. HCF data measured from notch specimens at R = 0.3 (20 °C, 100 Hz).

Best fit logarithmic trend lines are superimposed for the individual alloy data sets generated at R = −1, with a step test and associated interpolated endurance strength defined at 10^7 cycles in each case, Figure 6. The slope of the four individual stress–life curves was reasonably similar with a clear succession in HCF strength noted between the four alloys.

The construction of a best fit trend was inappropriate for Alloy A characterised at R = 0.3, Figure 7. Three constant amplitude, single stress tests performed on Alloy A failed with a life falling between 8.4 and 9.8 million cycles, under applied peak stress levels ranging between 450 and 500 MPa respectively (i.e., defining a counter-intuitive relationship between applied stress and fatigue life). These three tests were supplemented with two tests which ran out at 10^7 cycles and so generated interpolated endurance points in both cases. Notably, the two step tests failed at endurance levels lower than the single stress tests.

RR11 performed relatively well at R = 0.3 by attaining strengths comparable to some Alloy A tests. However, RR11 also displayed significant scatter in measured strength which again prohibited the construction of a suitable SN trend. Two single stress, constant amplitude tests straddle the endurance strength as defined from an interpolated step test.

No obvious explanation can be offered for the anomalous behaviour of Alloy A and RR11 at the R = 0.3 condition (i.e., the extensive scatter in SN performance). Some potential factors can be discounted. For instance, the specimens from all four alloys were manufactured ahead of the current matrix of testing as a single batch, using well established computer encoded machining techniques and associated tooling. The surface finish within the notches of all specimens was identical at R_A = ±0.5 µm. No differences in the surface residual stresses induced by machining can be expected between the four alloys. Notably, no similar issues with Alloy A and RR11 were evident at R = −1. Unfortunately, no further specimens were available to explore the issue in specific detail and generate a SN trend spanning a larger range in failure lives.

3.3. Fracture Surface Analysis

Fractography presented in Figure 8 (selected from Alloy B) and Figure 9 (Alloy A) exemplify the general forms of fracture generated in the plain and notch specimens respectively. Figure 8a illustrates a flat region of mainly transgranular fatigue crack growth perpendicular to the cyclic tensile axis, initiating from near the bottom of the image and propagating towards the top to form a teardrop shaped region in the central body of the specimen. Shear lips were formed at approximately ±45° to the opposing flanks during tensile overload. In this example, the precise site for crack initiation was found 150 µm beneath the gauge surface, Figure 8b. However, the detailed form of initiation was obscured in this case due to local asperity contact damage of the fracture surface resulting from the through zero R = −1 loading. It is probable that such compressive abrasion was active from the earliest stages of micro-crack formation and subsequent propagation.

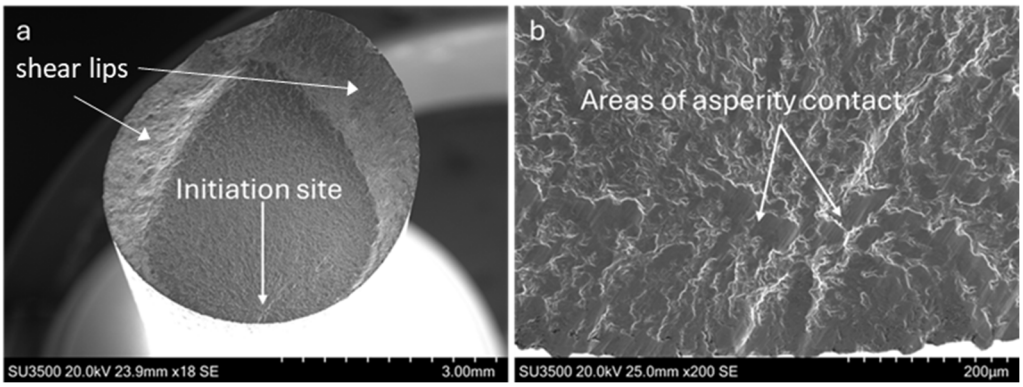

Figure 8. (**a**) Macroscopic fatigue failure in a plain specimen; (**b**) near-surface crack initiation site with features obscured by asperity contacts (Alloy B, σ_{max} = 550 MPa, N_f = 8,369,200, R = −1).

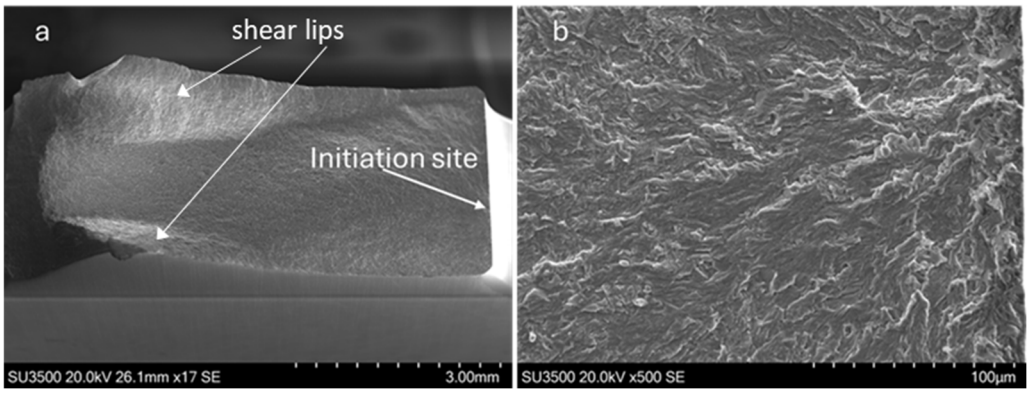

Figure 9. (**a**) Macroscopic fatigue failure in a notch specimen; (**b**) near-surface crack initiation site midway along notch root (Alloy A, σ_{max} = 450 MPa, N_f = 8,847,300, R = 0.3).

Crack initiation in the double notch specimens invariably occurred from one notch only and inboard along the notch root (i.e., away from the notch edges, due to the deburring applied during specimen manufacture), Figure 9a. This example, taken from an Alloy A specimen, illustrates the flat, mainly transgranular region of crack growth (right to left) through the mid-region of the net section, with ±45° shear lips formed along both lateral flanks plus the opposite notch during tensile overload. In this case, in the absence of compressive loading and therefore no asperity contact damage, it was possible to identify crack initiation from a heavily faceted region at approximately 20 µm below the right-hand notch root surface, Figure 9b.

All locations and morphologies of the crack initiation sites were catalogued from the individual specimens. Initiation site locations fell into three general groups: surface (depth 0–30 μm below the specimen surface), near-surface (depth 30 μm to 300 μm below the specimen surface) and sub-surface (depth > 300 μm).

Crack initiation sites in Alloy A, Alloy B and RR11 specimens of both geometries were dominated by near-surface or sub-surface locations, with fracture occurring from either isolated or clusters of primary α facets, Figure 10. Although EBSD measurements were not taken from the faceted primary α grains exposed on the present fracture surfaces, where this has been conducted in the past for a variety of near α and α/β titanium variants the facets typically form on basal or near basal planes of the α grains [34,35]. From observation at least, any differences in the chemical composition between the alloys under investigation here do not appear to affect the faceting mechanism. Very occasionally, notch specimens in Alloy A and Alloy B initiated from the notch root surface itself. Extensive areas of compressive asperity contact damage were evident for all specimens loaded through zero under R = −1, Figure 11.

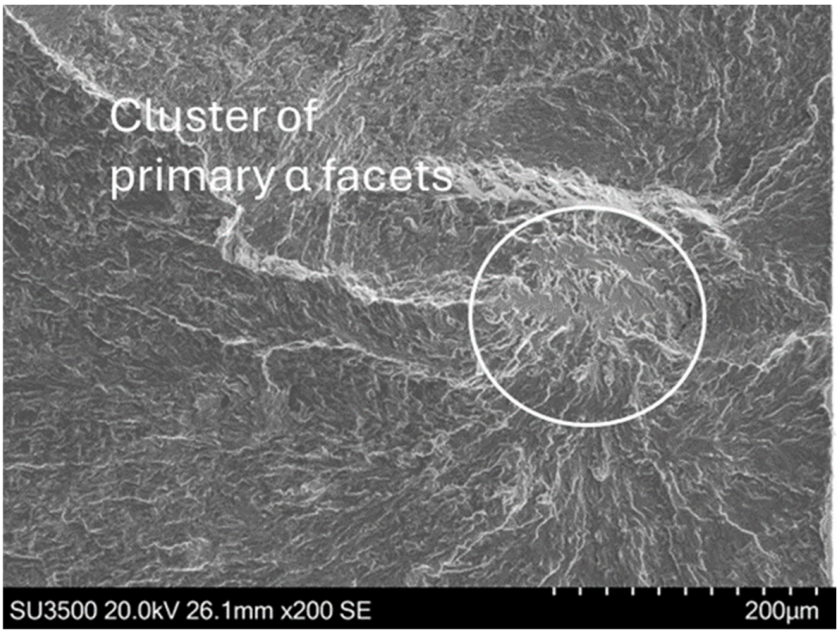

Figure 10. Example of sub-surface crack initiation from a cluster of primary α facets in RR11 (notch specimen, σ_{max} = 480 MPa, N_f = 7,724,900, R = 0.3).

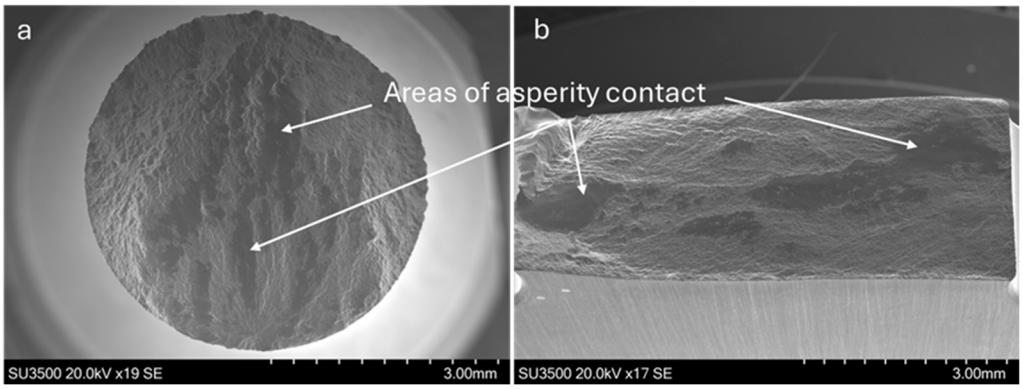

Figure 11. Extensive asperity contacts in RR11: (**a**) plain specimen (σ_{max} = 550 MPa, N_f = 7,722,900, R = −1); (**b**) notch specimen (σ_{max} = 311 MPa, N_f = 2,235,500, R = −1).

The precise location of crack initiation in RR11 specimens occasionally revealed underlying microstructural details reflecting the transformed secondary α structure adjacent to primary α grains, containing fine-scale lath structures at random orientations, Figure 12. These regions appeared inclined to the tensile loading axis.

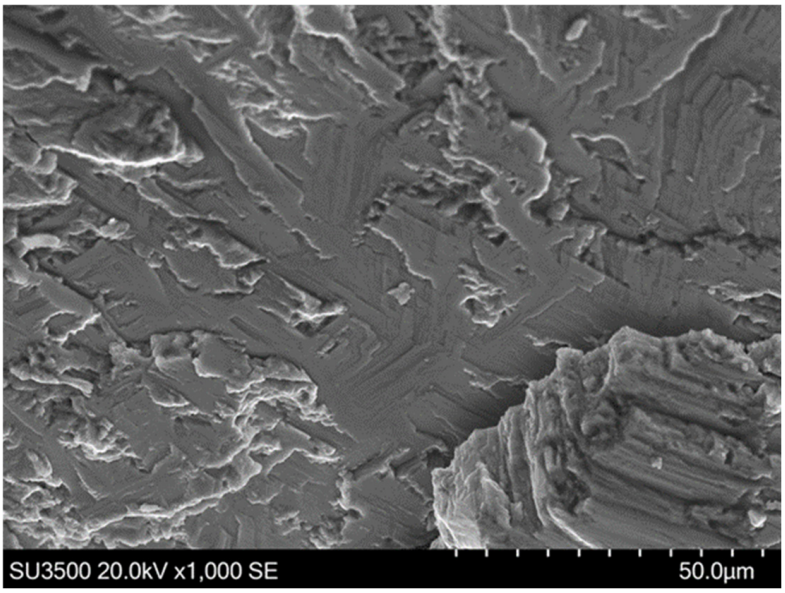

Figure 12. Secondary α region underlying the site of crack initiation in a RR11 plain specimen (σ_{max} = 575 MPa, N_f = 8,809,600, R = 0.3).

Due to the relatively coarse grain size and inherent primary α lath structures, the general appearance of the S23 fracture surfaces were distinct, even to the naked eye. All S23 specimens, whether plain or notch geometries, failed from near-surface or sub-surface locations and invariably displayed facets or inclined, angular features reflecting the primary α colony structures, Figure 13. Areas of compressive asperity contact were again common in S23 specimens undergoing R = −1 loading, but in this alloy the areas of contact were more isolated/less continuous and distributed across the fracture surface, Figure 14.

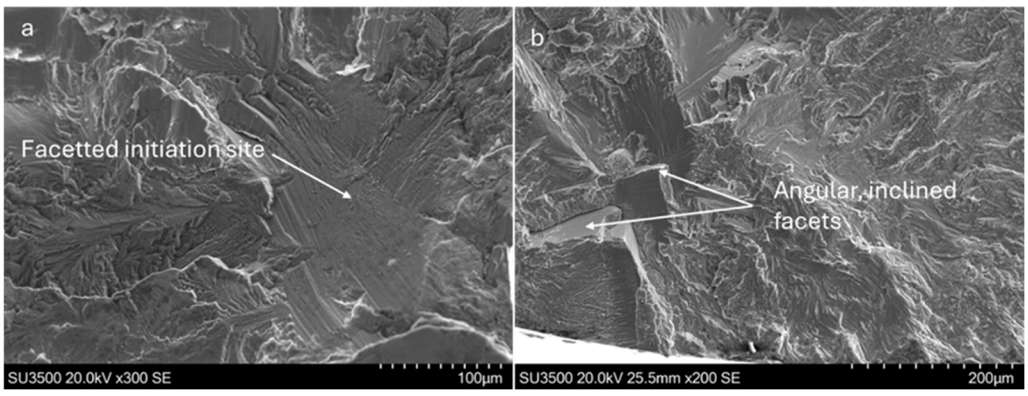

Figure 13. Examples of crack initiation in S23 alloy: (**a**) faceted initiation site in a notch specimen (σ_{max} = 275 MPa, N_f = 3,076,700, R = −1); (**b**) angular, inclined facets relating to α/β colony interfaces in a plain specimen (σ_{max} = 675 MPa, N_f = 875,200, R = 0.3).

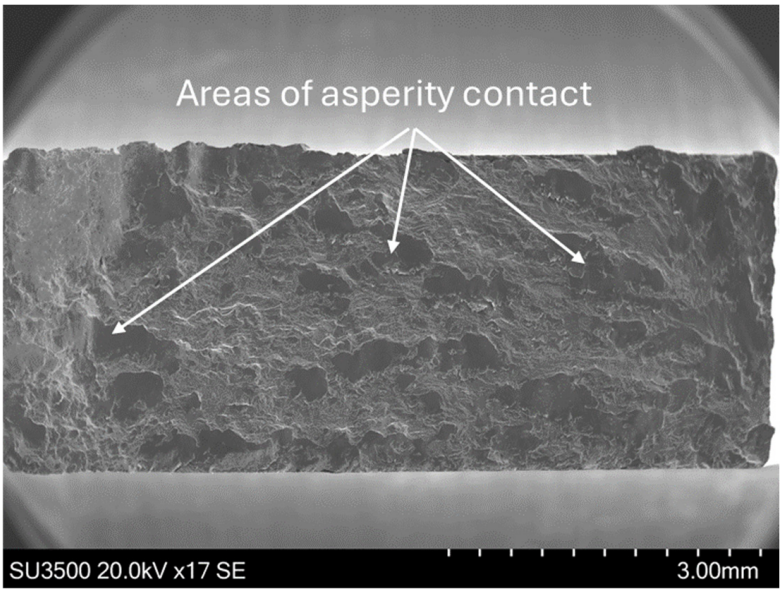

Figure 14. Isolated areas of compressive asperity contact distributed across the fracture surface in a S23 notch specimen (σ_{max} = 275 MPa, N_f = 3,076,700, R = −1).

4. Discussion

It is noted that, primarily governed by the material stocks available, the definition of selected SN curves during the course of the study relied on an absolute minimum of individual HCF tests. This meant that no attempt to quantify the degree of scatter amongst the fatigue data via repeat testing was possible. However, qualitative observations can be made concerning relative mechanical performance. In terms of fundamental fatigue strength, Figures 4 and 5 illustrate the HCF performance of plain specimens and demonstrate the superiority of the two commercially produced α + β alloys over the recently developed S23 and RR11. This duplicates one of the major conclusions from previous LCF experiments on the same four alloys [16]. Because of the employment of different mean stress conditions it was not possible to directly correlate the LCF and HCF data sets across the two studies.

Concentrating on the developmental alloys alone, when considering the plain specimen HCF data, the relative HCF performance of RR11 and S23 remains unproven. This is certainly true at R = −1 due to the differing decades in life to failure that have been generated, Figure 4, plus the potential cross cutting SN relationships. At R = 0.3, however, an obvious succession between the relative strengths of each alloy was evident. RR11 clearly outperformed S23 under notch specimen HCF testing, Figures 6 and 7. In fact, a notable performance was evident from RR11 at R = 0.3, matching or even exceeding the endurance strength of selected Alloy A specimens as measured at 10^7 cycles.

It could be argued that resulting from inappropriate selections of peak stress applied to the majority of plain S23 specimens throughout the present study, the measured lives to failure often fell short of a true HCF response, Figures 4, 5 and 7 (i.e., N_f~10^6 cycles or lower). The performance of the S23 notch specimens, however, reiterated the low HCF strength of the S23 material which, notably, contained the coarsest microstructure. It is widely accepted that fatigue crack growth resistance dominates fatigue life in the LCF regime. Hence, the coarse grain size in S23 should be beneficial for damage tolerance under LCF. At the opposite end of the stress–life curve, approaching the endurance condition, the crack initiation phase consumes a dominant proportion of the total life. The well established Hall–Petch (H-P) relationship would predict lower static yield strength for coarse grained metallic systems in general [36,37] and more recent studies have also correlated H-P models to fatigue behaviour, for example in commercially pure titanium [38]. Therefore, the

generally low fatigue and endurance strengths of S23 from this study are consistent with H-P models relating grain size to fatigue strength under HCF.

In contrast, any control on HCF strength by micro-texture was not so consistent throughout this study. The two commercial variants, Alloy A and Alloy B, often demonstrated similar fatigue performance (and even static strength) despite clear differences in texture, measured at 5.8 and 1.7 times random respectively, Table 1.

As previously described from testing under LCF and dwell fatigue conditions [16], the initiation sites of all the alloys were again dominated by quasi-cleavage facets: where failures initiated from isolated primary α grains (or clusters) in the bimodal alloys and packets of aligned α lath colonies in S23, as illustrated in Figures 12 and 13. This is not unexpected as facets formed near to or on basal planes are commonly seen at the fatigue initiation sites of α + β titanium alloys, where either surface or sub-surface crack initiation results from the micro plastic deformation caused by planar slip acting on restricted slip systems [34,35,39,40]. The stress redistribution and subsequent faceting mechanism is sensitive to grain size and in particular continuous slip band length, hence some of the most obvious facets were found in S23, Figure 15. The fact that faceting persisted under the R = −1 waveform suggests that the dislocation pile ups considered as a pre-requisite for stress redistribution and load shedding are not reversed as a result of through zero stress reversals.

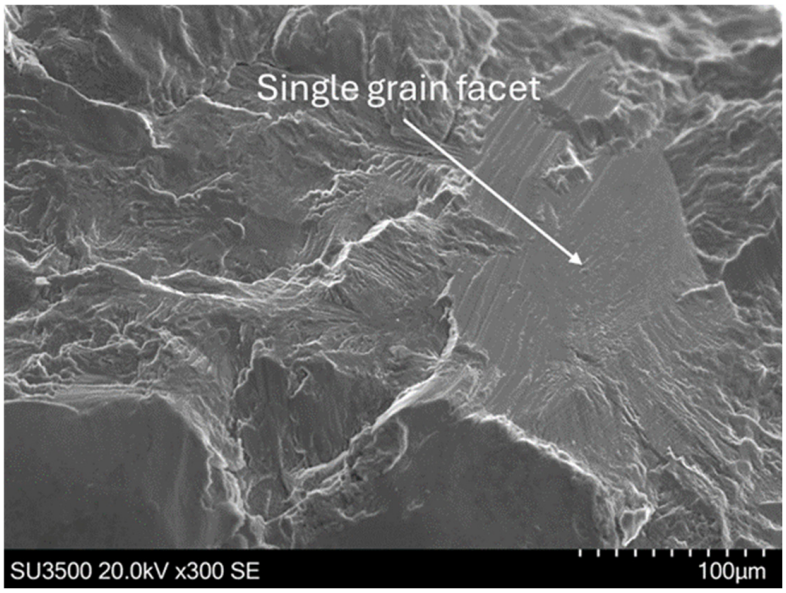

Figure 15. Facet correlating to a large, single grain containing α lath colonies in S23 alloy (plain specimen, σ_{max} = 400 MPa, N_f = 1,101,700, R = −1).

The coarse grain size of S23 was also responsible for the distinctive roughness to the fracture surfaces, as viewed by eye even without magnification. A mix of transgranular and intergranular fracture, the latter probably encouraged by the extensive grain boundary α phase, Figure 16, promoted localised and distributed asperity contacts during the compressive half cycle of the R = −1 waveform. In contrast, the three fine grained alloys (Alloy A, Alloy B and RR11) generated relatively smooth, transgranular fracture surfaces and compressive loading was accommodated across wider areas of contact.

The HCF data plotted in Figures 4–7 were employed to construct range-mean (RM) diagrams for plain and notch specimens relating to the specific combinations of peak to peak stress range and mean stress associated with the endurance strength defined at a fatigue life of 10^7 cycles. In order to define the relevant RM data, if step test data were available the endurance strength of that alloy was calculated employing the interpolation

technique from Equation (1). The reliance on step tests and the interpolation technique has previously been demonstrated as a cost effective but accurate method of defining endurance stress under HCF loading [33]. During the present study it proved invaluable for instances where the SN curve was defined by a minimum two points (for example see data for Alloy A in Figure 5 and S23 in Figure 6), negating the need to rely on extrapolating a best fit though two individual data points. However, in the absence of a relevant step test, the logarithmic best fit trends calculated from the single stress, constant amplitude data sets for each individual alloy, specimen geometry and R ratio were extrapolated to 10^7 cycles. The data employed to define endurance strength for each alloy, R ratio and specimen combination are specified in Table 3.

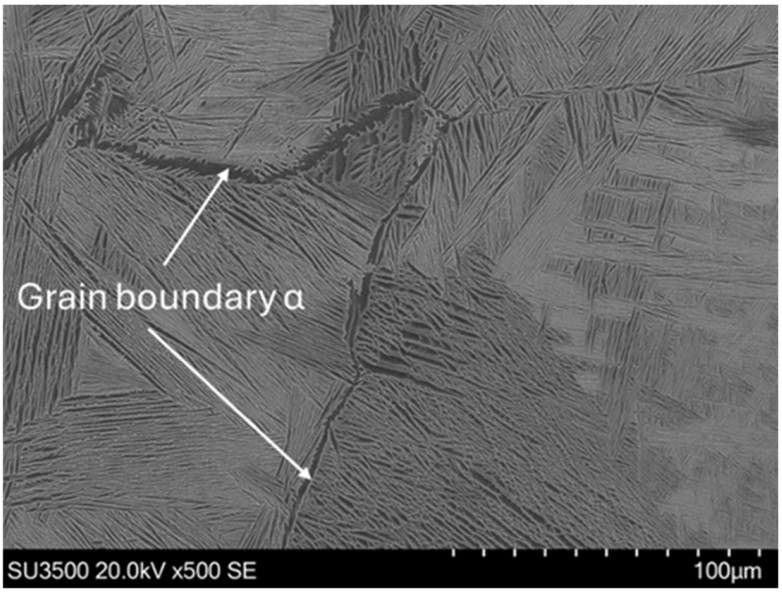

Figure 16. Continuous grain boundary α phase in S23 alloy.

Table 3. Endurance strength data employed as the basis of RM diagrams.

	R Ratio	σ_{peak} [MPa] Extrapolated from Single Stress Tests	σ_{peak} [MPa] Interpolated from Step Tests (Equation (1))
Plain specimens			
Alloy A	−1	524	-
	0.3	-	785
Alloy B	−1	518	-
	0.3	-	608
RR11	−1	-	325
	0.3	-	561
S23	−1	336	-
	0.3	481	-
Notch specimens			
Alloy A	−1	-	348
	0.3	-	406 ①
Alloy B	−1	-	343
	0.3	-	385
RR11	−1	-	292
	0.3	410 ②	-
S23	−1	-	258
	0.3	-	396

① lowest strength from an interpolated step test. ② lowest strength from a single stress test.

The first of these diagrams concentrating on the plain specimens and employing data at both R ratios, Figure 17, demonstrates that Alloy A and RR11 produced a near straight Goodman line. Alloy B and S23 displayed a moderate depression in the positive mean stress regime to produce "Haigh"style curves.

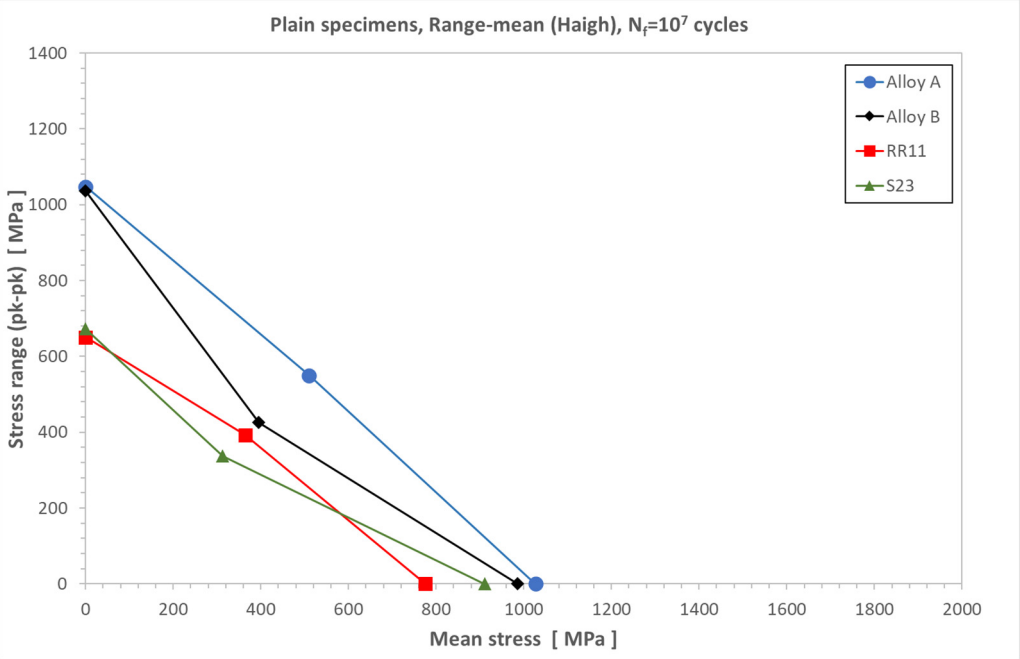

Figure 17. Range-mean diagram for plain specimens (N_f = 10^7 cycles).

RM plots were also constructed from the notch specimen data. Here bulk elastic loading was assumed by multiplying the applied net section stress by the notch K_t factor (K_t = 1.92). Initially, a pure Goodman approach was adopted in recognition of the adverse scatter noted from Alloy A and RR11 specimens at the positive R = 0.3 condition. Therefore Figure 18 utilised the HCF endurance measurements taken at R = −1 and the material proof strengths only. This emphasises the superior, near equivalent, performance of the two commercial alloys when compared to the developmental materials.

The alternative Haigh-style plot, Figure 19, utilised the additional endurance measurements taken from R = 0.3. In this case, legitimate measurements from interpolated step tests were available from the Alloy B and S23 materials. However, a significant degree of interpretation was necessary for Alloy A and RR11. In both cases a conservative engineering approach was taken. For Alloy A the datapoint at peak stress of 406 MPa was used, i.e., the lowest endurance strength interpolated from a step test. For RR11 a peak stress of 410 MPa was utilised, conforming to the lowest strength test that actually failed after 8.4 million cycles at that single stress condition. When viewing the SN data plotted in Figure 7 we believe this can be defended as a pragmatic approach. However, it is clear that further definition of the precise SN behaviour of Alloy A and RR11 would be essential as part of future test campaigns. The resulting Haigh curves reflected clearly different strengths at the two extremes of the relationship, i.e., for HCF endurance under R = −1 and the static proof strength. However, at the positive mean stress condition of R = 0.3, each alloy generated a similar RM strength that helped emphasise the Haigh-style behaviour.

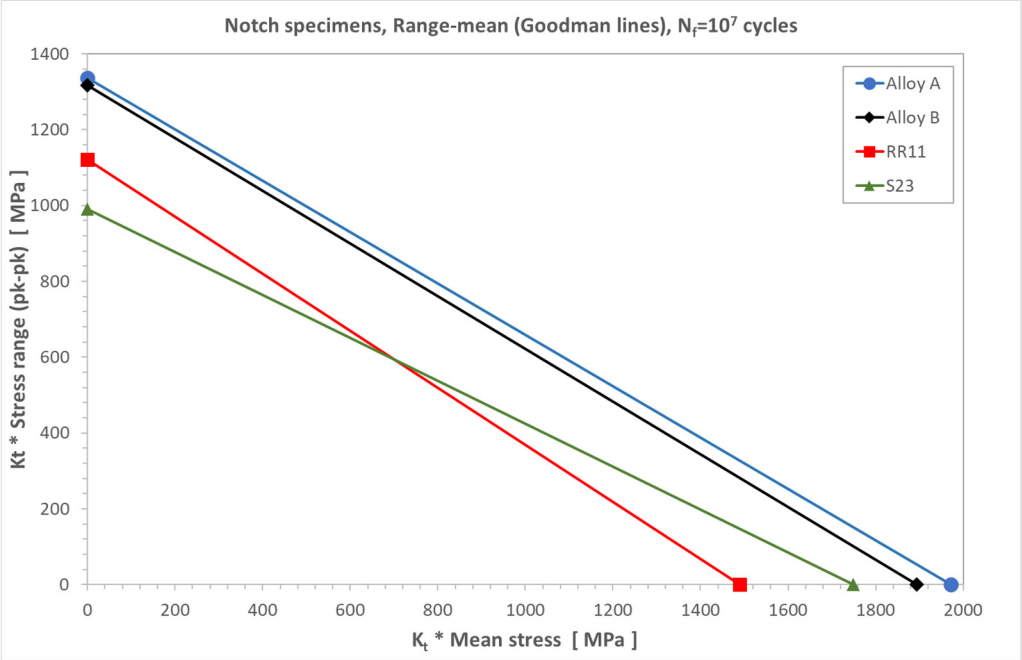

Figure 18. Goodman style range-mean diagram for notch specimens (i.e., with R = 0.3 data excluded), (N_f = 10^7 cycles).

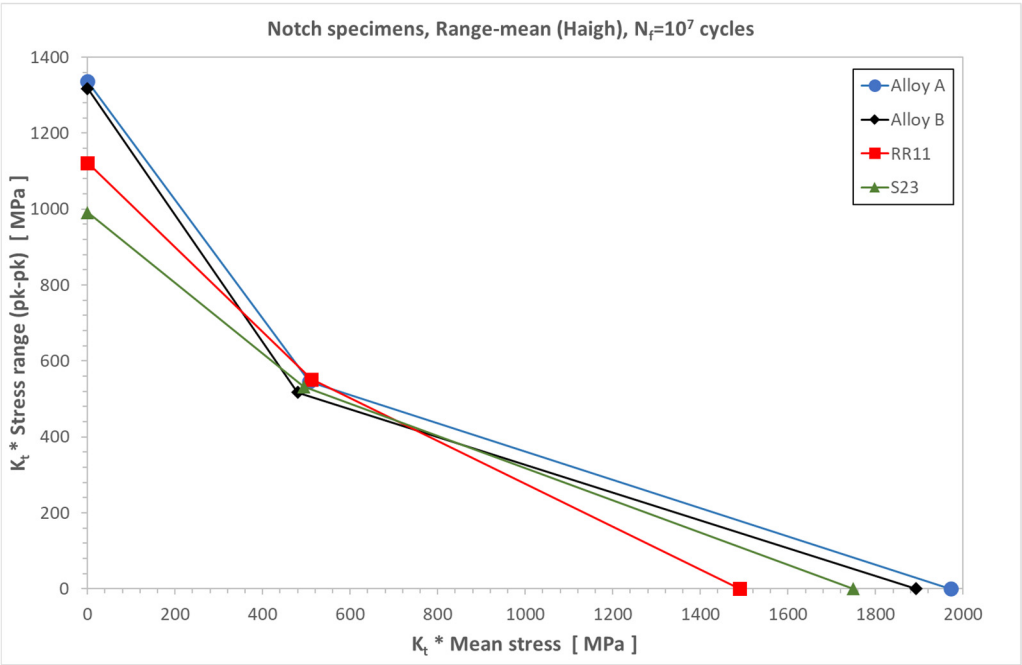

Figure 19. Haigh-style range-mean diagram for notch specimens (i.e., including R = 0.3 data) (N_f = 10^7 cycles).

The importance of generating fatigue data at multiple R ratio conditions was emphasised by comparing Figures 18 and 19. Reliance on a single fatigue data set at R = −1, Figure 18, would clearly over estimate the performance of all four alloys under intermediate mean stress conditions. Indeed, it is also argued that the RM Haigh curves in Figure 19 were constructed from a minimum number of fatigue mean stress conditions (i.e., R = −1 and R = 0.3), together with the 0.2% proof strength. Future testing is necessary to create a greater number of R ratio data sets in order to more accurately define the overall RM Haigh curve behaviour, even to the extent of including highly negative load ratios.

The promising HCF strength noted from the RR11 notch specimens was further emphasised when comparing the current findings to legacy RM data generated in the same laboratory and employing the same notch specimen geometry manufactured from two product forms of Ti-6-4 [41]. Both cross rolled plate and forged Ti-6-4 variants offered a weaker response compared to RR11 (and also S23) with marked depressions to the former RM trends, Figure 20. The propensity of Ti-6-4 to display such anomalous RM behaviour and sensitivity to mean stress has been previously reported [26,42,43]. Notably, our former RM testing on Ti-6-4 employed a greater number of different mean stress conditions to define the Haigh curves. A more comprehensive collection of different Ti-6-4 products has also been tested by way of ongoing RM studies and it has been concluded that the extent of the RM depression can be promoted by increasing grain size and high volume fractions of transformed β phase [41].

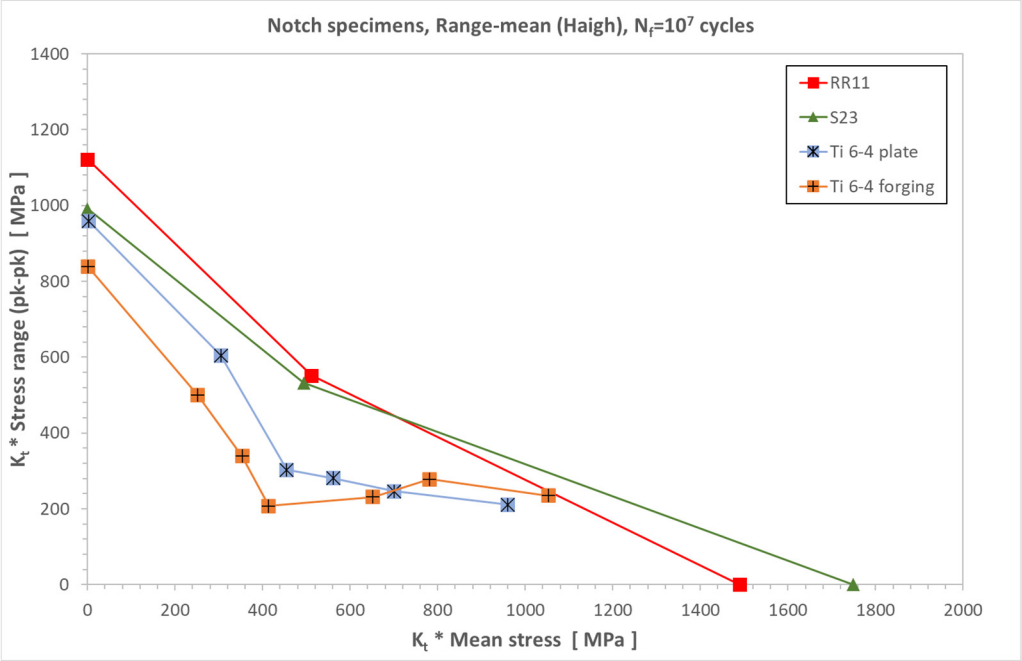

Figure 20. RM response of RR11 and S23 compared to two Ti-6-4 products, notch specimens (all K_t = 1.92).

Depending on potential engineering application, fatigue behaviour into the so-called VHCF or giga-cycle regime should be considered by extending the current RM Haigh curves to represent lives of 10^8 and even 10^9 cycles. A previous report on Ti-6-4 (mill annealed bar stock) has highlighted the pertinence of this approach. In that study, through the employment of an ultrasonic mechanical test rig, a bulk fatigue endurance strength as low as 340 MPa was reported at 10^9 cycles as opposed to the 600 MPa limit formerly indicated by more standard HCF testing when run-out was defined as 10^7 cycles [44]. Interestingly, a propensity towards sub-surface fatigue failures was also noted by the same study.

Differences in the relative performance of the four alloys under investigation, previously under LCF [16] and now HCF conditions, have highlighted some key points for future consideration. Increases in β phase stabilisation clearly offer improvements to both static and fatigue strength. The comprehensive alloy development and process optimisation programmes applied to the two commercial materials, Alloy A and Alloy B, were invariably reflected in superior fatigue strength. Improvements to the fatigue properties of both developmental materials, S23 and RR11, would be required to match these commercial counterparts, with options for microstructural and micro-texture modifications already

identified. However, it could be argued that S23 and RR11 in their current stage of development already offer unique potential for selected engineering applications. The processing of S23 from revert materials and powder blends makes this a particularly attractive material from the point of view of sustainable, cost-effective component manufacture. The promising HCF notch performance of RR11 could be matched to selected applications where LCF resistance and associated dwell performance [16] are not key design factors. In any case, with respect to both S23 and RR11, further metallurgical and processing optimisiation will be conducted. In addition, our knowledge of damage tolerant fatigue behaviour in this class of $\alpha + \beta$ titanium alloys has yet to be concluded. Experiments based on small and long fatigue crack growth, crack growth thresholds, plus fracture toughness are considered essential prior to eventual alloy selection.

5. Conclusions

An assessment of four $\alpha + \beta$ titanium alloys has been conducted under HCF loading. Each of the four alloys contained a relatively high volume fraction of β stabilising elements when compared to Ti-6-4. This HCF study supplements a previous study focussed on LCF properties and the potential for dwell sensitive fatigue behaviour [16]. The highlights from the present study were:

- Two commercial alloys, designated Alloy A and Alloy B, generally offer superior HCF strength compared to the two developmental alloys S23 and RR11. Using standard plain specimen SN data as an indication, Alloy A was typically the strongest, up to approximately 200 MPa greater when compared to S23 and RR11, for tests displaying fatigue lives between 10^6 and 10^7 cycles.
- Crack initiation in all four alloys is dominated by the formation of quasi-cleavage facets, most often located at sub-surface sites.
- Although S23 was stronger than RR11 under LCF, its performance is compromised in the HCF regime by a relatively large grain size.
- Range-mean (RM) diagrams were constructed as an aid to defining safe combinations of stressing under HCF conditions. It is acknowledged that the extent of the database and associated scatter in SN performance made the definition of endurance strength problematic on occasions. Where necessary a conservative engineering approach was taken.
- Range-mean behaviour of plain specimens indicates the two developmental alloys are approximately 30% weaker than the commercial competition at $R = -1$ and $R = 0.3$.
- From notch specimen data, all four alloys illustrated a marked depression in their RM diagram, thereby demonstrating a Haigh-style response. The importance of testing at multiple R ratio conditions was highlighted and the current Haigh curves should be supplemented by data at additional R ratios into the future.
- Continued metallurgical and process optimisations are recommended for S23 and RR11 whilst gathering additional knowledge of VHCF giga-cycle behaviour and defect tolerant performance.

Author Contributions: Conceptualization, P.D., H.D., C.C., N.M., K.F. and R.S.; methodology, P.D., C.C., N.M., K.F. and R.S.; validation, P.D., S.J. and H.D.; formal analysis, P.D., S.J. and M.B.; investigation, P.D. and S.J.; data curation, P.D.; writing—original draft preparation, P.D.; writing—review and editing, P.D., H.D., C.C., N.M., K.F., R.S. and M.B.; resources, C.C., N.M., K.F. and R.S.; project administration, H.D.; funding acquisition, H.D. All authors have read and agreed to the published version of the manuscript.

Funding: This research was conducted under the UK Aerospace Technology Institute (ATI) BETA project, application number: 10052028.

Data Availability Statement: The original contributions presented in this study are included in the article. Further inquiries can be directed to the corresponding author.

Acknowledgments: The provision of materials and supporting information from Rolls-Royce plc is gratefully acknowledged. S23 and RR11 materials were supplied by M. Jackson of Sheffield University and D. Dye of Imperial College respectively. Fatigue tests were performed at Swansea Materials Research and Testing Ltd. (SMaRT).

Conflicts of Interest: Authors Kate Fox, Christopher Collins, Nigel Martin and Rebecca Sandala were employed by the company Rolls-Royce plc at the time of writing. The remaining authors declare that the research was conducted in the absence of any commercial or financial relationships that could be construed as a potential conflict of interest.

Abbreviations

The following abbreviations are used in this manuscript:

EBSD	Electron back scatter diffraction
FAST	Field-assisted sintering technology
HCF	High cycle fatigue
H-P	Hall-Petch
ISM	Induction skull melted
LCF	Low cycle fatigue
NHCF	Notch high cycle fatigue
PAR	Plasma arc melted
PM	Powder metallurgy
RM	Range-mean
SEM	Scanning electron microscopy
SN	Stress-life
VAR	Vacuum assisted remelting
VHCF	Very high cycle fatigue

References and Note

1. Williams, J.C.; Boyer, R.R. Opportunities and Issues in the Application of Titanium Alloys for Aerospace Components. *Metals* **2020**, *10*, 705. [CrossRef]
2. Lütjering, G.; Williams, J.C. *Titanium*, 2nd ed.; Springer: Berlin/Heidelberg, Germany, 2007.
3. Boyer, R.R. An overview on the use of titanium in the aerospace industry. *Mater. Sci. Eng. A* **1996**, *213*, 103–114. [CrossRef]
4. Venkatesh, B.D.; Chen, D.L.; Bhole, S.D. Effect of heat treatment on mechanical properties of Ti-6Al-4V ELI alloy. *Mater. Sci. Eng. A* **2009**, *506*, 117–124. [CrossRef]
5. Semiatin, S.L.; Knisley, S.L.; Fagin, P.N.; Zhang, F.; Barker, D.R. Microstructure evolution during alpha-beta heat treatment of Ti-6Al-4V. *Metall. Mater. Trans. A* **2003**, *34*, 2377–2386. [CrossRef]
6. Mahore, S.; Tripathi, A.; Sharma, S. Property enhancement and microstructural evolution during thermo-mechanical processing of titanium alloys: A review. *Interactions* **2024**, *245*, 308. [CrossRef]
7. Semiatin, S.L. An overview of the thermomechanical processing of α/β titanium alloys: Current status and future research opportunities. *Metall. Mater. Trans. A* **2020**, *51*, 2593–2625. [CrossRef]
8. Ismaeel, A.; Xu, D.; Li, X.; Zhang, J.; Yang, R. Effect of texture on the mechanical and micromechanical properties of a dual-phase titanium alloy. *J. Mater. Res. Technol.* **2023**, *27*, 6833–6846. [CrossRef]
9. Lütjering, G. Influence of processing on microstructure and mechanical properties of (α+β) titanium alloys. *Mater. Sci. Eng. A* **1998**, *243*, 32–45. [CrossRef]
10. Peters, M.; Gysler, A.; Lütjering, G. Influence of texture on fatigue properties of Ti-6Al-4V. *Metall. Mater. Trans. A* **1984**, *15*, 1597–1605. [CrossRef]
11. Peters, M.; Kumpfert, J.; Ward, C.H.; Leyens, C. Titanium alloys for aerospace applications. *Adv. Eng. Mater.* **2003**, *5*, 419–427. [CrossRef]
12. Leyens, C.; Peters, M. (Eds.) *Titanium and Titanium Alloys: Fundamentals and Applications*; Wiley-VCH Verlag GmbH & Co.: Weinheim, Germany, 2003. [CrossRef]

13. Mateo García, A.M. BLISK Fabrication by Linear Friction Welding. In *Advances in Gas Turbine Technology*; IntechOpen: Rijeka, Croatia, 2011; pp. 411–435. [CrossRef]
14. Kumar, B.V.R.R. A Review on BLISK Technology. *Int. J. Innov. Res. Sci. Eng. Technol.* **2013**, *2*, 1353–1358.
15. James, S.; Gudipati, P.; Kantor, A.; Phillips, J. Near-to-net titanium extrusions as a substitute for aerospace plate and forgings. In *Proceedings of the 15th World Conference on Titanium (Ti-2023), Edinburgh, UK, 12–16 June 2023*; Institute of Materials, Minerals and Mining (IoM3): London, UK, 2023.
16. Davies, P.; John, S.; Davies, H.; Bache, M.; Fox, K.; Collins, C.; Martin, N.; Sandala, R. The Low-Cycle Fatigue Performance of Emerging Titanium Alloys for Aeroengine Applications. *Metals* **2025**, *15*, 1274. [CrossRef]
17. Ritchie, R.O.; Davidson, D.L.; Boyce, B.L.; Campbell, P.; Order, O. High-cycle fatigue of Ti-6Al-4V. *Fatigue Fract. Eng. Mater. Struct.* **1999**, *22*, 621–631. [CrossRef]
18. Umezawa, O.; Morita, M.; Yuasa, T.; Morooka, S.; Ono, Y.; Yuri, T.; Ogata, T. Analyses of heterogeneous deformation and subsurface fatigue crack generation in alpha titanium alloy at low temperatures. *AIP Conf. Proc.* **2014**, *1574*, 34–41. [CrossRef]
19. Pyttel, B.; Schwerdt, D.; Berger, C. Very high cycle fatigue—Is there a fatigue limit? *Int. J. Fatigue* **2011**, *33*, 49–58. [CrossRef]
20. Gao, T.; Zhao, X.; Xue, H.; Sun, Z. Characteristics and micromechanisms of fish-eye crack initiation of a Ti-6Al-4V alloy in very high cycle fatigue regime. *J. Mater. Res. Technol.* **2022**, *21*, 3140–3153. [CrossRef]
21. Nicholas, T. Critical issues in high cycle fatigue. *Int. J. Fatigue* **1999**, *21*, S221–S231. [CrossRef]
22. Döker, H. Fatigue crack growth threshold: Implications, determination and data evaluation. *Int. J. Fatigue* **1997**, *19*, S145–S149. [CrossRef]
23. Ritchie, R.O.; Boyce, B.L.; Campbell, J.P.; Roder, O.; Thompson, A.W.; Milligan, W.W. Thresholds for high-cycle fatigue in a turbine engine Ti–6Al–4V alloy. *Int. J. Fatigue* **1999**, *21*, 653–662. [CrossRef]
24. Lee, Y.L.; Taylor, D. Stress-Based Fatigue Analysis and Design. In *Fatigue Testing and Analysis: Theory and Practice*; Elsevier Butterworth-Heinemann: Burlington, MA, USA, 2004; pp. 103–180. [CrossRef]
25. Sendeckyj, G.P. Constant life diagrams—A historical review. *Int. J. Fatigue* **2001**, *23*, 347–353. [CrossRef]
26. Oberwinkler, B. On the anomalous mean stress sensitivity of Ti-6Al-4V and its consideration in high cycle fatigue lifetime analysis. *Int. J. Fatigue* **2016**, *92*, 368–381. [CrossRef]
27. Nicholas, T. *High Cycle Fatigue: A Mechanics of Materials Perspective*; Elsevier Ltd.: London, UK, 2006.
28. Liao, D.; Zhu, S.-P.; Correia, J.A.; De Jesus, A.M.; Berto, F. Recent advances on notch effects in metal fatigue: A review. *Fatigue Fract. Eng. Mater. Struct.* **2020**, *43*, 637–659. [CrossRef]
29. Lister, S.; Baxter, G.J.; Jackson, M. Titanium-S23: A New Alloy with Ultra-High Tensile Toughness Directly from the Solid-State Processing of Recycled Ti–6Al–4V and Ti–5Al–5Mo–5V–3Cr Powders using Field Assisted Sintering Technology. *Adv. Eng. Mater.* **2025**, *27*, 2500572. [CrossRef]
30. Weston, N.S.; Thomas, B.; Jackson, M. Processing metal powders via field assisted sintering technology (FAST): A critical review. *Mater. Sci. Technol.* **2019**, *35*, 1306–1328. [CrossRef]
31. Rolls-Royce plc. Titanium Alloy and Method of Manufacture. European Patent EP4640859A1, 29 October 2025. Available online: https://worldwide.espacenet.com/patent/search/family/091275161/publication/EP4640859A1?q=EP4640859A1 (accessed on 1 August 2025).
32. *BS EN 2002-1:2005*; Aerospace Series. Metallic Materials. Test Methods—Tensile Testing at Room Temperature. British Standards Institution (BSI): London, UK, 2005.
33. Bellows, R.S.; Muju, S.; Nicholas, T. Validation of the step test method for generating Haigh diagrams for Ti–6Al–4V. *Int. J. Fatigue* **1999**, *21*, 687–697. [CrossRef]
34. Li, J.; Davies, H.M.; Fox, K.; Mulyadi, M.; Glavicic, M.G.; Bache, M.R. An appraisal of dwell sensitive fatigue in Ti-6Al-4V and the governing role of inhomogeneous micro-texture. *Int. J. Fatigue* **2023**, *171*, 107589. [CrossRef]
35. Bache, M.; Davies, H.; Davey, W.; Thomas, M.; Berment-Parr, I. Microstructural Control of Fatigue Behaviour in a Novel α + β Titanium Alloy. *Metals* **2019**, *9*, 1200. [CrossRef]
36. Armstrong, R.W. Engineering science aspects of the Hall–Petch relation. *Acta Mech.* **2014**, *225*, 1013–1028. [CrossRef]
37. Chong, Y.; Deng, G.; Gaoa, S.; Yi, J.; Shibata, A.; Nobuhiro, T. Yielding nature and Hall-Petch relationships in Ti-6Al-4V alloy with fully equiaxed and bimodal microstructures. *Scr. Mater.* **2019**, *172*, 77–82. [CrossRef]
38. ALkhazraji, H.; El-Danaf, E.; Wollmann, M.; Wagner, L. Enhanced Fatigue Strength of Commercially Pure Ti Processed by Rotary Swaging. *Adv. Mater. Sci. Eng.* **2015**, *2015*, 301837. [CrossRef]
39. Li, W.; Umezawa, O. A review of subsurface crack initiation models in high-cycle fatigue for titanium alloys. In *Key Engineering Materials*; Trans Tech Publications Ltd.: Zurich, Switzerland, 2017; pp. 76–81. [CrossRef]
40. Liu, C.; Thomas, R.; Sun, T.; Donoghue, J.; Zhang, X.; Burnett, T.L.; Quinta da Fonseca, J.; Preuss, M. Multi-dimensional study of the effect of early slip activity on fatigue crack initiation in a near-α titanium alloy. *Acta Mater.* **2022**, *233*, 117967. [CrossRef]
41. Rolls-Royce. Private data, 2002.

42. Lindemann, J.; Wagner, L. Mean stress sensitivity in fatigue of α, (αβ) and β titanium alloys. *Mater. Sci. Eng. A* **1997**, *234–236*, 1118–1121. [CrossRef]
43. Adachi, S.; Wagner, L.; Lütjering, G. Influence of microstructure and mean stress on fatigue strength of Ti–6Al–4V. In *Titanium '84—Science and Technology*; Lütjering, G., Zwicher, U., Bunk, W., Eds.; Deutsche Gesellschaft für Metallkunde: Oberusel, Germany, 1985; Volume 4, pp. 2139–2146.
44. Atrens, A.; Hoffelner, W.; Duerig, T.W.; Allison, J.E. Subsurface Crack Initiation in High Cycle fatigue in Ti6Al4V and in a Typical Martensitic Stainless Steel. *Scr. Metall.* **1983**, *17*, 601–606. [CrossRef]